The Planetary Science Journal, 4:126 (15pp), 2023 July https://doi.org/10.3847/PSJ/acd1ef
© 2023. The Author(s). Published by the American Astronomical Society.
OPEN ACCESS

Global Mapping of Fragmented Rocks on the Moon with a Neural Network: Implications for the Failure Mode of Rocks on Airless Surfaces

Ottaviano Rüsch[1] and Valentin T. Bickel[2,3]
[1] Institut für Planetologie, Westfälische Wilhelm Universität Münster, Münster, Germany
[2] Center for Space and Habitability, University of Bern, Bern, Switzerland
[3] ETH Zurich, Zurich, Switzerland
Received 2022 December 8; revised 2023 April 27; accepted 2023 April 27; published 2023 July 17

Abstract

Failure modes of lunar boulders depend both on rheology and the erosion agents acting in the lunar surface environment. Here, we address the failure modes of lunar boulders and their variations at a quasi-global scale (60°N to S). We deploy a neural network and map a total of ∼130,000 fragmented boulders (width > ∼10 m) scattered across the lunar surface and visually identify a dozen different disintegration morphologies corresponding to different failure modes. Our findings suggest that before a boulder is catastrophically shattered by an impact, there is an internal weakening period with minor morphological evidence of damage at the rock scale at the resolution of the used imagery. We find that some of the rare pre-shattering morphologies (e.g., fractures) are equivalent to morphologies observed on asteroid Bennu, suggesting that these morphologies on the Moon and on asteroids are likely not diagnostic of their formation mechanism (e.g., meteoroid impact, thermal stresses). In addition, we identify new morphologies such as breccia boulders with an advection-like erosion style. We publicly release the produced fractured boulder catalog along with this paper.

Unified Astronomy Thesaurus concepts: Selenology (1441); Planetary geology (2288); The Moon (1692)

1. Introduction

Fracturing, fragmentation and fragment size frequency distribution (SFD) resulting from impact-induced failure of solids are aspects relevant for a wide range of studies (e.g., Kun & Herrmann 1999). In the case of failure of rocks, these aspects provide information about rock strength and are studied for engineering applications and geological research (e.g., Hogan et al. 2012; Zhang et al. 2022). The process of collision and fragmentation is key for the evolution of planetesimals, asteroids, and solid surfaces (e.g., Capaccioni et al. 1986; Housen & Holsapple 1990; Giblin et al. 1998; Ryan & Melosh 1998; Tanga et al. 1999; Durda et al. 2007). The role of impact fragmentation for the evolution of solid surfaces is increasing in relevance since it is known that properties of boulder-rich planetary surfaces can deviate from those covered by fine-grained regolith. This has motivated studies of contact, impact, and cratering processes in targets composed of coarse to very large particles (e.g., Cintala et al. 1999; Güttler et al. 2012; Tatsumi & Sugita, 2018; Barnouin et al. 2019; Kadono et al. 2019; Arakawa et al. 2020; Ballouz et al. 2020; Lauretta et al. 2022; Okawa et al. 2022; Ormö et al. 2022; Raducan et al. 2022a; Stickle et al. 2022; Walsh et al. 2022; Daly et al. 2023). As particle size increases, the impact kinetic energy available for particle shattering increases, until there is no energy left for crater excavation: in such a case, only a shattered or pit-hosting particle (boulder) is left (e.g., Durda et al. 2011) that effectively armors and protects the surface from excavation. For such surfaces, dominated by multicrystal rocks and boulders, the boulder shattering process—and thus the boulder failure mode—becomes relevant. Here we use the term "boulder" following the definition of Dutro et al. (1989), i.e., size >25.6 cm, and not the more strict definition of size in the range 0.1–1 m (Bruno & Ruban 2017) used elsewhere (e.g., Ruesch et al. 2020). There are few opportunities to directly observe the highly dynamic shattering process at the appropriate conditions or to observe the outcomes of naturally occurring fragmentation. However, fragmented lunar boulders represent a unique opportunity to observe the aftermath of such natural events.

Instances of rock failures due to meteoroid bombardment have been observed on the Moon using orbital images acquired by the Lunar Reconnaissance Orbiter Narrow Angle Camera (LROC/NAC; Ruesch et al. 2020). The exact impact conditions (impactor number, angle, mass, size, and velocity) for each instance of boulder shattering are not known, only probability functions are available. Nevertheless, the very slow geological erosion on the Moon, with respect to that on Earth, allows observations of the pristine morphology (e.g., fragments position and shape mostly unmodified by later mass wasting) after failure, even if the shattering event leading to failure occurred several tens of million years ago. The study of Ruesch et al. (2020) investigated about ∼1000 blocks of size above ∼10 m all located around four large impact craters. It demonstrated that the majority of instances of shattered rocks are due to meteoroid bombardment and that the morphology of failed rocks, despite being highly variable, does not vary with surface exposure time. Furthermore, the study discussed whether some morphologies of lunar boulders might be attributable to stresses from diurnal temperature variations. In fact, thermal stresses can play a role in weakening and perhaps potentially breaking lunar rocks at the micro and/or macro scale. The effects of diurnal temperature variation on the lunar surface are a function of the complex spatiotemporal properties of the stress fields and thus on the rock size, composition, shape, and location (Molaro et al. 2017). These effects have been the subject of recent studies (Ravaji et al. 2019; Hörz et al. 2020; Patzek & Rüsch 2022).

Original content from this work may be used under the terms of the Creative Commons Attribution 4.0 licence. Any further distribution of this work must maintain attribution to the author(s) and the title of the work, journal citation and DOI.

Several questions follow from the first morphological study of lunar rock failures with LROC/NAC (Ruesch et al. 2020). Are the previously identified morphologies representative of boulder failure modes across the surface of the Moon, or do the failure modes vary selenographically? How do the lunar boulder failure modes compare to recent observations of failure modes on other bodies, specifically on near Earth asteroids Itokawa (e.g., Nakamura et al. 2008), Bennu (e.g., Molaro et al. 2020; Cambioni et al. 2021; Delbo et al. 2022), and Ryugu (e.g., Sugimoto et al. 2021)?

This study uses a neural network on LROC/NAC images (Robinson et al. 2010) in order to search for fragmented blocks on a quasi-global scale (60°N to S), scanning through ∼150,000 images. Similar (global-scale) machine-learning-driven searches were previously performed by Bickel et al. (2020a) and Bickel et al. (2022). In addition to mapping applications, earlier work used machine learning for global-scale analyses of the physical surface properties of the Moon and asteroids, such as performed by Cambioni et al. (2019), Kodikara & McHenry (2020), and Moseley et al. (2020). Our neural network was trained on images that cover the full range of known block degradation states, including boulders with single fracture, heavily fractured boulders, as well as catastrophically shattered boulders, specifically excluding large, intact boulders. The resulting network is capable of identifying fractured media from the meter- to hecto-meter scale.

2. Method

Our methodological approach consists of four main steps: (1) neural network training and validation, (2) neural network–driven detection and mapping, (3) candidate clustering, and (4) visual inspection and review.

2.1. Neural Network Training and Validation

We utilized a convolutional neural network architecture called RetinaNet (Lin et al. 2017) with a ResNet50 backbone that has been successfully deployed for a series of lunar machine-learning mapping-related studies in the past (Bickel et al. (2020a, 2021a, 2018)). Using NAC images used by previous studies of fractured boulders (e.g., Ruesch et al. 2020) as well as randomly selected images, a total of 151 positive and 67 negative training labels were manually created by a human operator following previously established procedures (Bickel et al. 2020b, 2021b). Here, a label consists of a rectangular bounding box drawn around the feature of interest. Training labels intentionally included a wide range of boulder disintegration states (Figure 1), ranging from boulders with single fractures to completely disintegrated boulders; intact boulders were specifically excluded, i.e., included as negative training labels. The neural network was trained over a total of 75 epochs (one epoch corresponds to one pass of the training data set through the model), utilizing label augmentation, specifically image flipping, rotation, re-sampling (+/−10%), shearing, and radiometric adjustments (brightness and contrast) to help avoid overfitting. The trained model achieves a recall of 58.8% and a precision of 90.9% in an independent and representative test set (5% of the training set, which was set aside before training). The relatively small size of the test set is driven by the overall lack of available labels. Here, the term "recall" describes the percentage of fractured boulders that were detected by the model in the test set, while the term "precision" describes the percentage of correct detections.

We note that the nature, distribution, physical appearance, and frequency of fractured boulders and outcrops on the Moon are not known exactly, which means that our training data set is likely not completely representative of the actual population of fractured boulders. Here, we approach this fundamental limitation by purposely training the network on an extremely wide range of boulder degradation states (using one single class; see Figure 1), forcing the network to generalize to a very wide range of boulder and fracture morphologies. The improved generalization of the network effectively broadens its perception, enabling it to identify not only known, but also previously unknown types of fractured boulders, which are not represented in the training set. In other words, this study utilizes an object detector (supervised learning) to perform a quasi-similarity search. Given that our network is not expected to be trained on the complete range of fractured boulder morphologies, we do not expect the testing scores to be representative of the actual performance of the network—this implies that the results of this study can only be considered in a qualitative way.

2.2. Neural Network–driven Detection and Mapping

We deployed the trained neural network in an existing LROC/NAC processing pipeline (Bickel et al. 2020a, 2022) on a number of Google Cloud virtual computing instances. The output of this pipeline includes a list of fractured feature candidate detections (here called "candidates"), with relevant information regarding location and size of features, as well as candidate preview patches, i.e., full-resolution thumbnails (∼100 by ∼100 pixels on average, with 0.5–1 m ground sampling dimension) of each candidate detection that are useful for review and science analysis. The training and deployment of the neural network was limited to images with incidence angles between 10° and 60° to avoid steep slopes to be shadowed (observational bias). This effectively prevented the neural network from scanning regions at latitudes higher than 60° N and S.

2.3. Clustering

The detected candidates represent objects of very different geological nature, such as fractured boulders and rocky craters. In addition, the network identified visually similar objects that are not (directly) geologically related to fractured boulders, such as craters and fracture sets in impact melt deposits. The sheer number and wide range of represented geomorphic features makes a systematic, human-driven analysis difficult. To facilitate human review and analysis, we used an unsupervised (saliency-based) clustering approach to sort all candidates in clusters that share certain visual characteristics. Specifically, we use a pre-trained (ImageNet) VGG16 to identify relevant features in the candidate images and a k-means approach to subsequently sort them into 15 clusters, in a completely unsupervised way. Here, 15 classes were identified as the best compromise between cluster uniqueness and diversity. We note that not each of the 15 clusters may be truly unique—there may be significant (human-perceived) overlap among clusters. We note that the object detector described above and the clustering algorithm are completely independent.

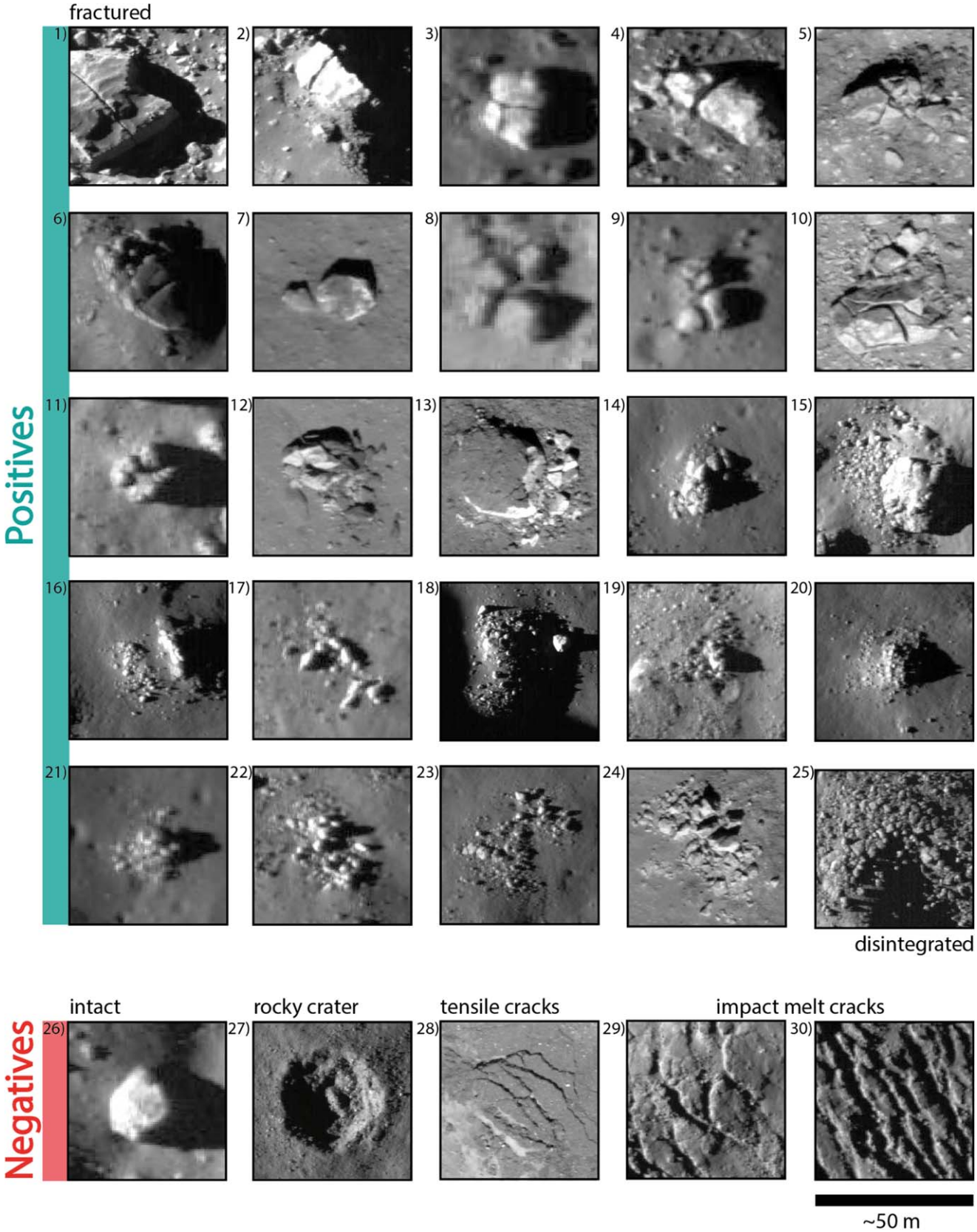

Figure 1. Examples of positive and negative labels used for the training of the neural network. Note how the full range of boulder disintegration is covered, from fractured all the way to catastrophically shattered (1 through 25). Negative labels include intact boulders, craters, and linear features unrelated to boulder disintegration (26–30). Image credits to NASA/LROC/GSFC/ASU.

2.4. Visual Inspection

One of the clusters predominantly consists of features not related to fractured boulders; we removed this cluster from further analysis. In each of the feature-positive, selected clusters we visually searched for recurring patterns in the morphology of the cluster of fragments. Practically, the analysis consisted in a rapid photogeological interpretation of the thumbnails (e.g., Wilhelms et al. 1987), i.e., (i) identification of discrete surfaces within the thumbnail, (ii) association of these surfaces to geological units (rocks, soils), and (iii) association of the units shades to three-dimensional shapes. Attention was paid to the number, size and shape of the fragments, the position of the fragments with respect to each other, and the presence of cracks. To characterize the fragments we use the ratio of the area of the largest fragment to the minimum polygon area enclosing all fragments (Alf/Ap). This metric approximately describes the size of the largest fragment to the size of the parent rock. Despite being influenced by the spreading of the fragments away from the impact location, this parameter is useful as a first-order morphometric descriptor. Values of this metric are reported for entire morphological types, not for single detections. Challenges of this data set, and of optical images in general, consist of the lack of topographic information and the presence of shadows that obliterate areal fractions of the scene. In order to avoid misinterpretation of morphologies, only morphologic types occurring at least twice are reported. Use of multiple images acquired at different local times could help to further improve the interpretation of the morphologies.

3. Results

3.1. Overview

The machine-learning algorithm identified a total of 187,787 fractured feature candidates, which were clustered into 15 individual clusters. After visual inspection, we found that 14 clusters predominantly contain features that are directly related to boulder fragmentation; one cluster predominantly contains features that are unrelated.

Of the 15 clusters, 14 are considered relevant for further investigation with a total of 159,442 features. Cluster 8 was disregarded. We note that clusters 0, 1, 3, 10, and 14 contain a substantial portion of crater-related features (containing 72,929 features), thus, are described as "heterogeneous." Due to the overwhelming number of candidates in each cluster, only about 50% of the detections in each relevant cluster are visually analyzed. A dozen morphological types are identified and are described in the next section. We note that several of these types are morphological end-members and that a continuum of morphologies is observed in between these end-members. The discarded cluster 8 predominantly contains fresh rocky and/or concentric craters. We include a summary table with cluster ID and overall representative features below (Figure 2). The produced catalog and candidate preview patches are available, free of charge, here: 10.48620/224

3.2. Maps

We produce a series of maps to visualize the spatial distribution and frequency of a number of particularly interesting clusters. Figure 3 shows cluster 2 contains mostly a few large (>∼7 m) fragments, cluster 8 contains predominantly impact craters, and cluster 13 contains mostly many small (<∼5 m) fragments. We note that clusters that predominantly contain impact craters appear to be scattered randomly, while clusters that predominantly contain fractured boulders appear to be systematically located. Globally distinct hotspots (spatial clusters) of fractured boulders are predominantly located in and around craters. Interestingly, fractured boulder hotspots are located in craters of almost all ages, ranging from Copernican- to Imbrian-aged craters. Hotspots of fractured boulders of different clusters—i.e., with different morphological properties—are not necessarily co-located; for example, Tycho features a prominent cluster of mostly a few large (>∼7 m) fragments, but not of many small (<∼5 m) fragments. Similarly, Mare Humorum features a significantly increased number of many small (<∼5 m) fragments, but an apparent lack of few large (>∼7 m) fragments (Figure 3). It is important to keep in mind that the used neural network suffers from a fundamental bias, which might result in potentially misleading maps.

3.3. Morphological Types

This section contains detailed qualitative descriptions of the fractured boulder morphologies we observed throughout the data set. These morphological types are found in one or several of the identified clusters.

Cavity (Figures 4(a), (b)): these instances are characterized by an intact boulder, i.e., without fractures, with one of the sides (hereafter facets) presenting a fracture plane curvilinear in planar view. The fracture plane is identifiable because it is partly in shadow. *Interpretation:* the fracture plane represents a cavity into the boulder. In one case, fragments the size of the cavity are located in the proximity of the cavity near the boulder and might represent excavated material from the cavity. A similar morphology has been reported on asteroid Bennu (Molaro et al. 2020). Whether this morphology on the Moon and on Bennu share the same formation process is discussed in Section 4.

Interrupted near-horizontal spalling (Figures 1(c), (d)): These boulders present narrow linear shadows that partly, not completely, cross a facet. There is no spatial displacement of the illuminated rock material on both sides of the linear shadow. *Interpretation*: the topography responsible for such shadow configuration can consist of a step-like relief where the topographically lower side is in shadow. Step-like relief can form by interrupted spallation when the energy necessary for spalling an entire slab is insufficient and the crack changes direction toward the nearest surface. The fragment removed by the spall is not visible because (i) it was displaced outside the frame, (ii) it has been shattered in small unrecognizable pieces, or (iii) occurred before the emplacement of the boulder at the current location. Similar morphology and interpretation has been reported by Nakamura et al. (2008). Unlike for the other morphologies, the formation of the features for this type can have occurred during formation of the block itself rather than post-emplacement. The presence of a vertical crack (deep incision) instead of an interrupted spall is excluded because the Sun-facing wall of the crack is missing. The Sun-facing wall is present in other morphologies (see interrupted fracturing).

Interrupted or deviated fracturing (Figures 4(e), (f)): These boulders present narrow linear or zig-zag shadows that partly or completely cross a facet. The illuminated sides juxtaposing the shadow do not have the same brightness and one side can be as bright as the brightest area of the image. *Interpretation:* the juxtaposing of shadow with relatively high brightness indicates

Cluster ID	Dominant archetype	No. of features	Mean est. diameter	Example
0	Heterogeneous cluster, large- to small-sized fractured boulders mixed with many fresh and rocky craters	14,206	8.9 m	
1	Heterogeneous cluster, mid- to small-sized fractured boulders with many fresh, rocky, and concentric craters	10,614	15.5 m	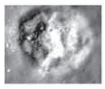
2	Homogeneous cluster, large- to mid-sized fractured boulders	6,852	10.9 m	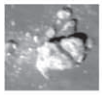
3	Heterogeneous cluster, large- to small-sized fractured boulders mixed with many fresh and rocky craters	17,863	11.1 m	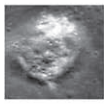
4	Homogeneous cluster, mid- to small-sized fractured boulders	14,103	8.2 m	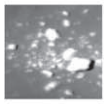
5	Homogeneous cluster, large- to mid-sized fractured boulders	13,084	7.8 m	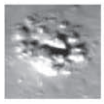
6	Homogeneous cluster, large- to mid-sized fractured boulders	11,025	8.2 m	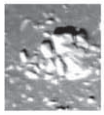
7	Homogeneous cluster, mid- to small-sized fractured boulders mixed with some fresh craters	11,288	13.0 m	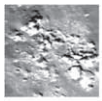
8	Homogeneous cluster, fresh, concentric, and rocky craters	28,345	7.9 m	
9	Homogeneous cluster, mid- to small-sized fractured boulders	8,009	9.9 m	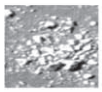
10	Heterogeneous cluster, large- to small-sized fractured boulders mixed with many fresh rocky craters and some intact boulders	18,650	8.1 m	
11	Homogeneous cluster, mid- to small-sized fractured boulders	8,765	8.2 m	
12	Homogeneous cluster, large- to small-sized fractured boulders	6,212	10.3 m	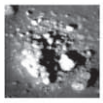
13	Homogeneous cluster, mid- to small-sized fractured boulders	7,175	8.3 m	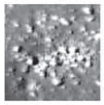
14	Heterogeneous cluster, large- to small-sized fractured boulders mixed with some fresh, rocky, and concentric craters	11,596	10.2 m	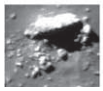

Figure 2. Summary of all produced clusters, including archetype description, number of features, mean estimated diameter of the feature (not of single fragments; using the approach described by Bickel et al. 2018), and an exemplary NAC crop-out. Note that the given example for heterogeneous clusters is not representative of the full range of features. The estimated mean diameter between cluster classes is above the implemented range of $+/-10\%$ scaling used in label augmentation, hence excluding that differences between boulder classes of similar archetype but different diameter are an artifact of label augmentation. Image credits to NASA/LROC/GSFC/ASU.

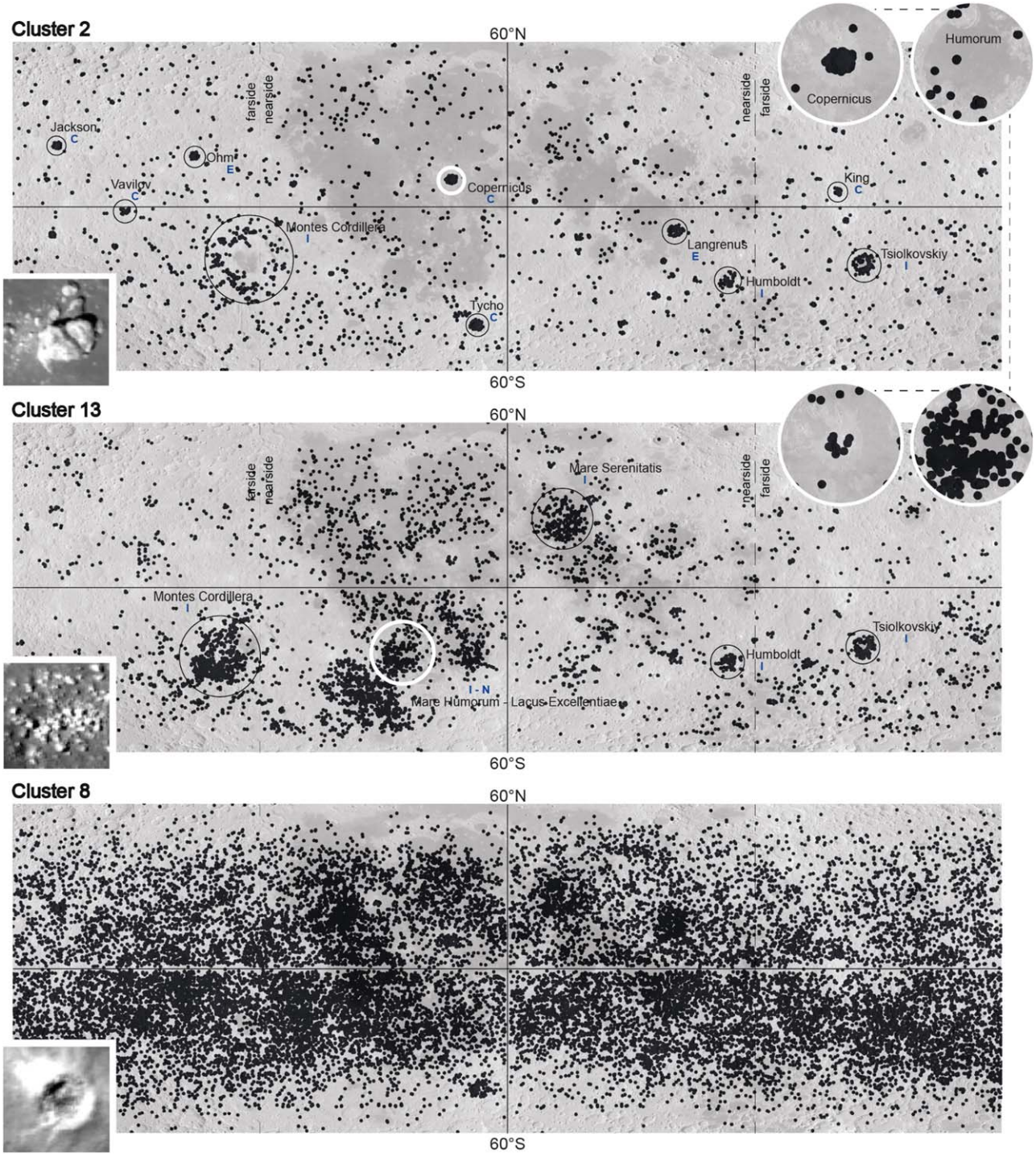

Figure 3. Spatial distribution of clusters 2 (predominantly large fractured boulders), 13 (predominantly small fractured boulders), and 8 (predominantly impact craters), shown as black dots. A few selected, globally distinct hotspots are highlighted by black circles; host location age is indicated by a single letter: C = Copernican, E = Eratosthenian, I = Imbrian, N = Nectarian. Insets show details of the Copernicus and Mare Humorum regions, indicated by white circles on the map. WAC global mosaic in the background; WAC image credits to NASA/LROC/GSFC/ASU.

a crack topography with a trough sufficiently deep and with steep wall. The illuminated steep wall can be responsible for the relatively high brightness next to the shadow. Crack depth and width are likely increased by a displacement of the newly created fragments. The zig-zag pattern can represent the deviation of the original crack propagation direction toward the nearest surface. Here the crack appears to propagate through the boulder, whereas in the interrupted spalling type, the crack affected the boulder only superficially.

Axial failure (Figures 4(g), (h)): Boulder with one or more narrow linear shadows of constant width running through an entire facet. In planar view, the contact between multiple shadows occurs predominantly at either an approximately right angle ($n = 5$) or at an angle in the range 30°–40° ($n = 6$). *Interpretation:* shadows resulting from near-vertical fractures. In some cases, fractures cut through the entire boulder height, and the resulting fragments are slightly displaced. As noted previously in Matsui et al. (1982), these fractures resemble axial

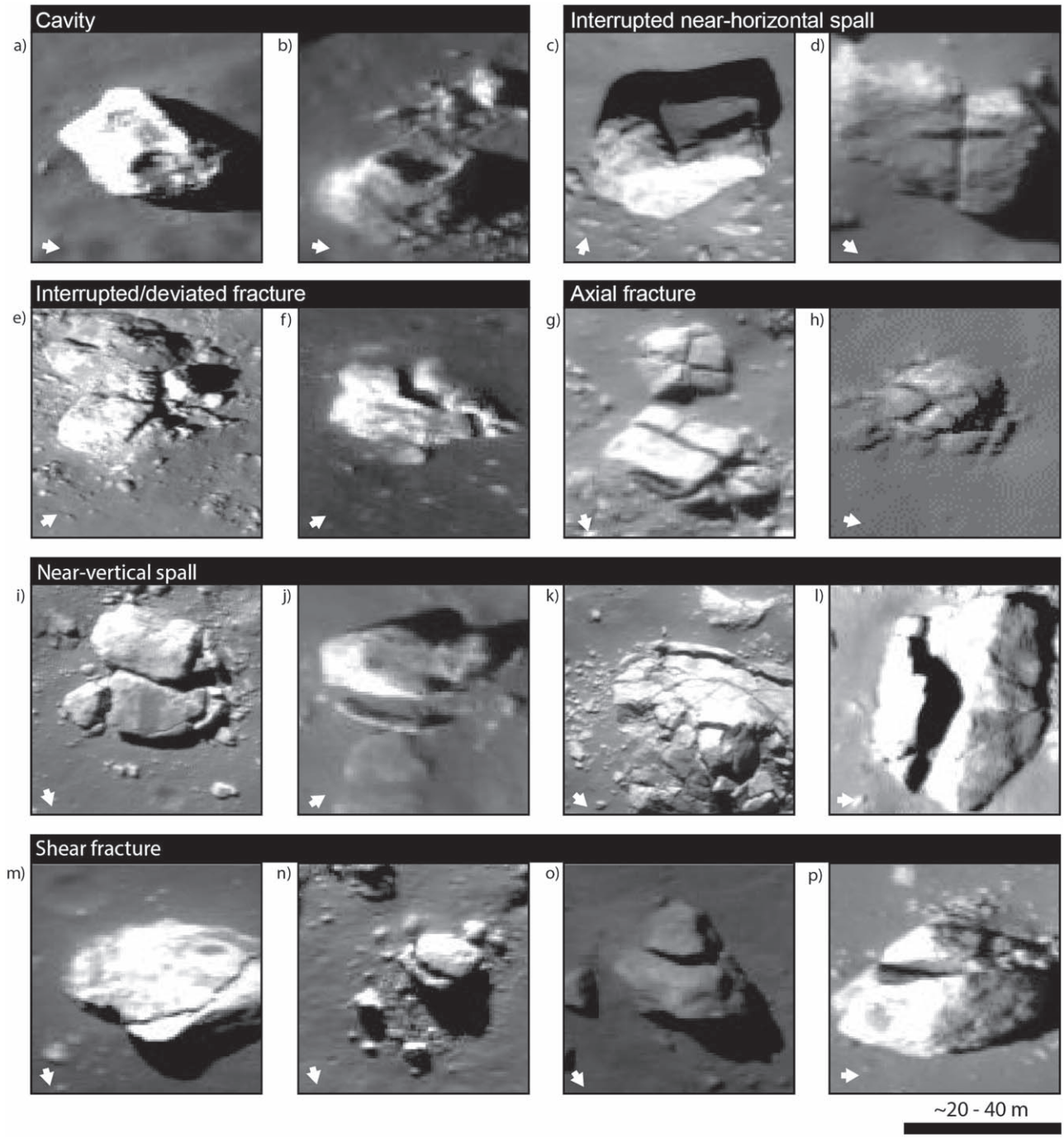

Figure 4. Examples of detections for different morphological types. The large arrow denotes illumination direction. Panel widths vary in the range 30–60 m. (a) M174889254LC, (b) M176602625RC, (c), M124999473RC, (d) M1251998743RC, (e) M152702349RC, (f) M126595195LC, (g) M1162548409LC, (h) M1221615756RC, (i) M1222952209LC, (j) M112671946LC, (k) M108292443LC, (l) M1296942537RC, (m) M170905869LC, (n) M172460917LC, (o) M157364573RC, (p) M175408129RC. Image credits to NASA/LROC/GSFC/ASU.

failures observed in static uniaxial compression tests (e.g., Basu et al. 2013) where a rock is split along one of its axes. This morphological type on the Moon was already reported in Ruesch et al. (2020) where it was suggested to be due to thermal stresses due to the nonrandom orientation of cracks. As discussed below, the new instances detected in this study suggest that single and multiple axial failures could also be part of a continuum of morphologies resulting from a wide range of imparted impact energy.

Near-vertical spalling (Figures 4(i)–(l)): in planar view, a narrow shadow runs near and parallel to the edge of a facet. In some places along its length, the shadow can increase in width and be juxtaposed to an illuminated boulder area of high brightness. *Interpretation:* these are examples of spalling of rocks where the largest surface of the spalled flake is oriented vertically. The flake can either be mostly attached to the parent block or located slightly away from it. This morphology bears strong similarity to the exfoliation morphology reported on Bennu (Molaro et al. 2020). The thickness of the proposed spalled flakes on Bennu relative to their parent boulder is much smaller than what is observed here. We note, however, that the resolution of the images for the Moon does not allow us to detect

thinner flakes. Whether this morphology on the Moon and on Bennu share the same formation mechanism is discussed in the discussion section.

Shear fracture (Figures 4(m)–(p))*:* Boulder presenting a curved narrow shadow of variable width, juxtaposed to a relatively bright illuminated area of rock. The narrow shadow separates the parent boulder in two fragments. The smaller fragment is not as small as in the case of near-vertical spalling. *Interpretation:* the curved pattern of the narrow shadow indicates that the dipping of the crack is not vertical but tilted, implying shear failure along a single plane that led to the partial superposition of two large fragments. Shear failure is a typical failure mode observed, for example, in compression tests (e.g., Basu et al. 2013).

Concentric fracturing (Figures 5(a), (b)): this type of morphology, as well as those that follow, is characterized by more than two fragments. The boundary of the central fragment presents a semicircular shadow. The configuration of the shadow bears resemblance to the shear failure type. In this type, however, more than two fragments are present and the central fragment can be rounded in planar view. *Interpretation:* the only resemblance with the literature of solid fragmentation is the presence of a fragment at a central location, i.e., surrounded by fragments on all sides, like in the so-called core shattering events (Fujiwara et al. 1989). Core shattering fragmentation can develop shell-like fractures surrounding the core (e.g., Fujiwara & Tsukamoto 1980; Durda et al. 2015) similar to the concentric fracturing observed here. In our examples, the characteristic is that the central fragment is round and that is not necessarily the largest fragment.

Core (Figures 5(c), (d)): this morphology is composed of a group of several fragments. One fragment has all its sides surrounded by other fragments. This fragment is located at a central location, i.e., other fragments are distributed around it in all directions and can, in some cases, be the largest. The number of relatively small fragments is variable. *Interpretation:* the central fragment is a core, i.e., a fragment whose facets are not the original outer surface of the parent block. This type of fragmentation can be associated with confidence to the core shattering type described by, e.g., Fujiwara et al. (1989), Fujiwara & Tsukamoto (1980), and Durda et al. (2015). The number of very small fragments is likely due to the age of the shattering event, i.e., high for recent events and low for old events (Rüsch et al. 2022). We cannot exclude, however, that shattering events producing only very few small fragments occur. Several instances of this group are very similar to the "concentric fracturing" type, implying a continuum of morphologies. There is a morphological resemblance to a boulder disaggregation instance reported on Bennu (Figure 5 in DellaGiustina et al. 2019).

Cluster (Figures 5(e), (f)): Group of fragments with the area of the largest fragment much smaller than the area covered by the group ($\mathrm{Alf}/\mathrm{Ap} < 0.1$). The number of fragments is >50. The cluster can have a concentration of fragments at its center or along a circle. Fragments can form rays radiating from the center of the cluster. The surface in between fragments can have a higher reflectance than the background surface away from the cluster. *Interpretation:* the ratio Alf/Ap can be used as a proxy for the ratio of the mass of the largest fragment to the mass of the parent target (e.g., Ruesch et al. 2020). Based on this parameter, the morphology corresponds to highly catastrophic events where the mass of the largest fragment is much smaller (<0.1) than the mass of the parent.

No core (Figures 5(g), (h)): This morphology is composed of several fragments. The positions of the largest fragments form a circular feature, i.e., it encircles an area lacking relatively large fragments. The center of the feature presents relatively very small or no fragments at all, effectively a "stone circle" landform. The number of relatively small fragments surrounding the large fragments is highly variable. *Interpretation:* this type is similar to the "core" type without the central fragment (the core). See the subsection "cluster" for a discussion of the very small fragments. An instance similar to this type is the Loong Rock (Outer Fence) group of fragments at the Chang'E-3 landing site (Li et al. 2015; Di et al. 2016; Li & Wu 2018). There is resemblance to a group in a "crude circle" configuration reported on Deimos (Figure 12B in Thomas 1979).

Cones (Figures 5(i)–(k)): This morphology is a group of fragments with one or more fragments displaying a triangular and/or elongated shape in planar view (cone-like) and with the apex located toward the center of the cluster. Unfortunately, it has not yet been possible to discern the entire three-dimensional shape of these elongated fragments; thus, while one aspect ratio is known to be very high ($a >> c$), we have no information on the other (relationship a,b). *Interpretation:* this morphology corresponds to the well-known "cone-type" fragmentation reported in Fujiwara et al. (1989), Matsui et al. (1982), Giblin et al. (1994), and Giblin et al. (1998). Elongated or flattened fragments are often formed on the outer target surface, especially in the cratering regime (Fujiwara et al. 1989; Nakamura et al. 2008; Walker et al. 2013). Here, however, the presence of these fragments near the center of the cluster and not on its edge, as well as their rather straight and not curvilinear form, is consistent with the formation of such fragments inside the parent target, as found by Durda et al. (2015). This type of morphology is consistent with dominant radial fracturing.

Bright zone (Figures 5(l)–(m)): Presence of a single high reflectance patch. Where the patch is relatively large, it is centered on a boulder fracture or a fragment edge. The reflectance of the patch is higher toward its center. The boundary of the patch is gradational and uncorrelated to fragment edges or other topography. There is no evident association to a specific morphological type of fractured or fragmented boulder. *Interpretation:* high reflectance is due to unweathered rock and soil surfaces typical for very recent exposures (e.g., Pieters & Noble 2016). The exposure of fresh material is likely due to a meteoroid impact (e.g., Hörz et al. 1975; Ruesch et al. 2020) with the patch corresponding to the spall zone on a rock and to adjacent ejecta material. Since the patches are observed to spatially coincide with a fracture or with the edges of juxtaposed fragments, they are direct evidence that a meteoroid event is responsible for the fracturing and fragmentation. This same co-occurrence of a fragmented boulder and brightening can be noted at White Rocks of station C1, Apollo 14 (Ruesch et al. 2020), possibly enhanced by the high albedo of the anorthitic petrology. Very similar white spots on blocks on Itokawa have been interpreted as resulting from meteoroid impacts (Nakamura et al. 2008).

Plate-like fragments (Figures 6(a), (b)): Relatively rare assemblage of fragments with one of the largest fragments of very high reflectance and with an abrupt transition between illuminated high-reflectance area and shadow. The bright fragment can display a relatively high ratio of shadow length to rock width. *Interpretation:* this configuration suggests the

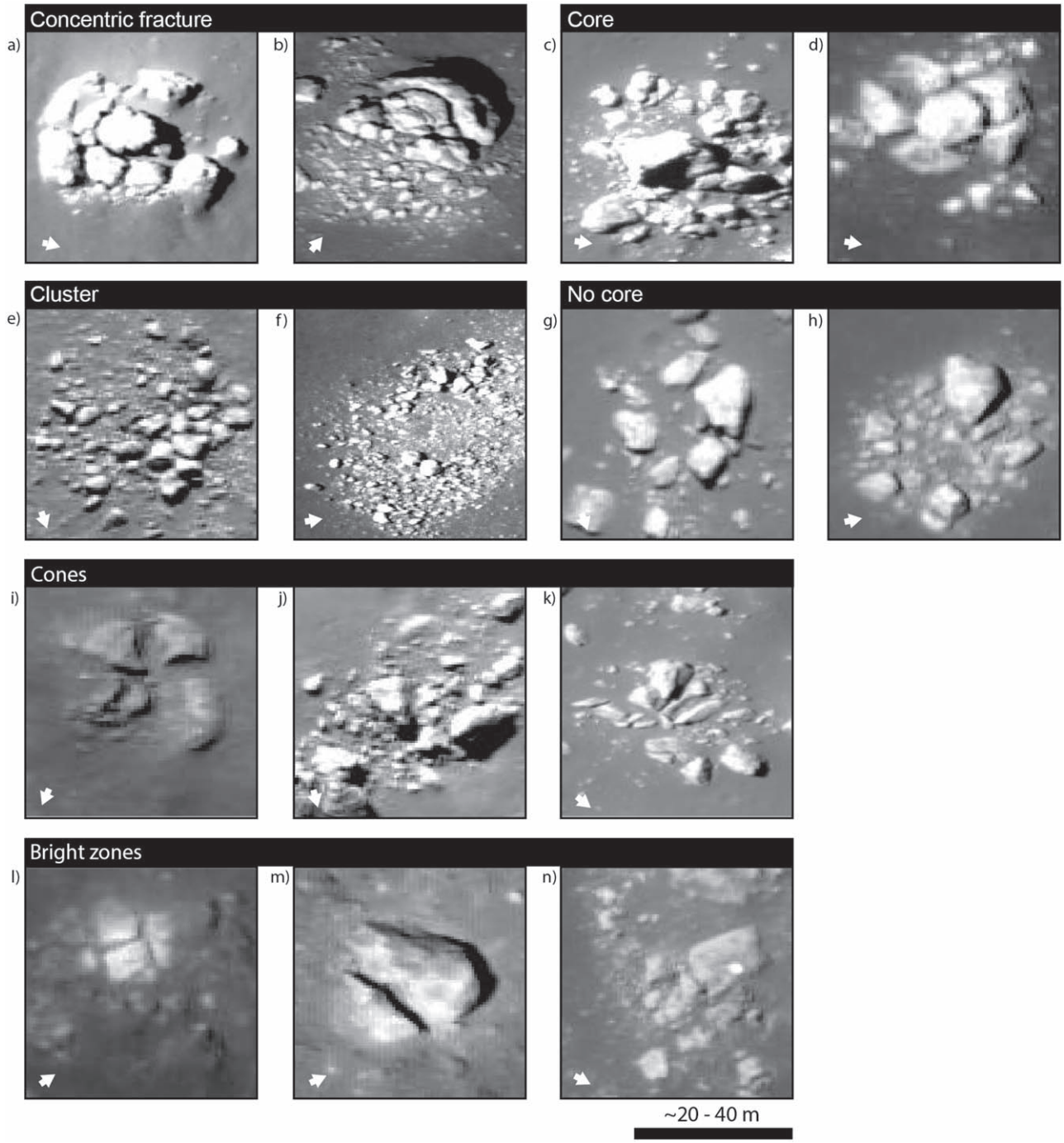

Figure 5. Examples of detections for different morphological types. The large arrow denotes illumination direction. Panel widths vary in the range 30–60 m. (a) M1356624061RC, (b) M169845868RC, (c) M127240244LC, (d) M108203484RC, (e) M109780793RC, (f) M168523403LC, (g) M1193830064LC, (h) M110560726RC, (i) M108366721LC, (j) M139029855LC, (k) M169283456RC, (l) M110560726RC, (m) M109895309LC, (n) M110526893RC. Image credits to NASA/LROC/GSFC/ASU.

presence of a plate-like fragment, with an inclined (∼40°–60°) side relative to the background surface. The spatial configuration of illuminated and shadowed surfaces indicates that the fragment forms an overhang. This overhang configuration is likely the result of the plate-like shape and the rather vertical position of the fragment. The high-reflectance surface is due to favorable scattering from the steeply inclined fragment side. Flattened fragments are rather common in solid fragmentation, as noted in literature (e.g., Durda et al. 2015) and in the morphological types described so far.

Partially buried (*putative*; Figures 6(c), (d)): These are boulders or fragments partially or completely inside a shallow depression. The shape of the depression can be circular or irregular. *Interpretation:* the co-occurrence of fragments in or near a crater-like depression can be a coincidence. Alternatively, it could represent impact-induced fragmentation of a partially buried boulder. As demonstrated experimentally, impact on a partially buried rock leads only to minimal damage and is associated with the formation of a main crater of circular to irregular-shaped and several smaller craters (Durda et al. 2011).

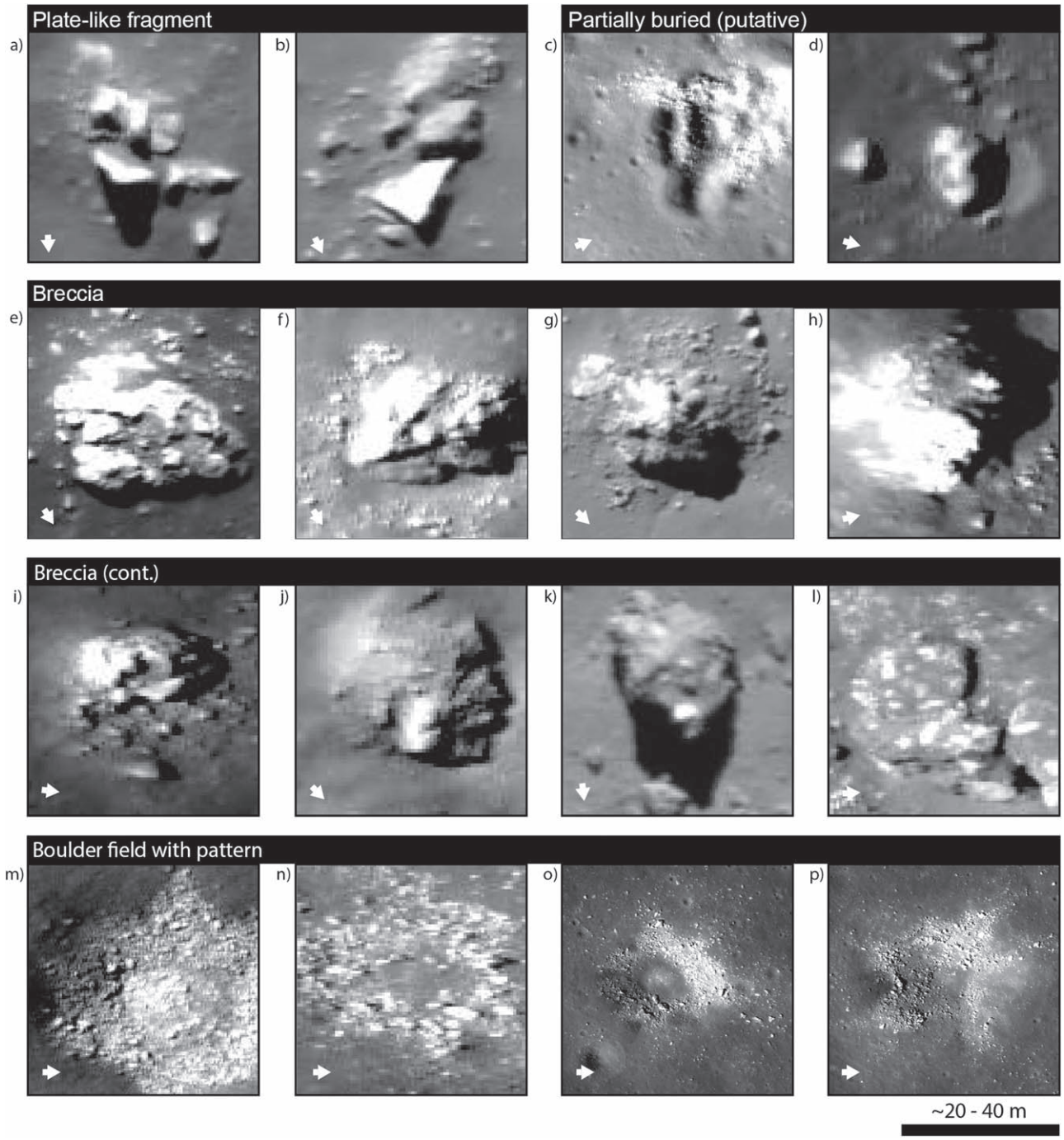

Figure 6. Examples of detections for different morphological types. The large arrow denotes illumination direction. Panel widths vary in the range 30–60 m. The view for the detections in (o,p) has been enlarged to 300 m width. (a) M1299030725RC, (b) M110649693RC, (c) M1280467964LC, (d) M1130300625RC, (e) M110126713LC, (f) M1325718594RC, (g) M111668133RC, (h) M137278395RC, (i) M168869503RC, (j) M107809965LC, (k) M1343664677RC, (l) M127070409LC, (m) M1221580467RC, (n) M168442030LC, (o,p) M137420922LC. Image credits to NASA/LROC/GSFC/ASU.

Breccia (Figures 6(e)–(l)): This is a morphology that does not present spatially resolved fractures or detached fragments and nevertheless show signs of disaggregation. These instances are characterized by heterogeneous reflectance of boulder facets together with a relatively small shadow on top of the main boulder facet. The heterogeneous reflectance forms several patches with sharp boundaries. Some of the patches have a shadow at their boundary. The boundary of the boulder is highly irregular and leads to partial enclosure of the juxtaposed soil (Figure 6(e)). The partial enclosures can extend into linear and curvilinear features on the facet of the boulder (Figures 6(f), (j)). These boulders are found on the rim of old ($>\sim$100 Myr) craters as part of a mature population of ejecta blocks. *Interpretation:* the patches represent clasts within a matrix, and the boulder thus constitute a breccia. The partial enclosures and linear to curvilinear features are evidence for incision and trough formation into the boulder where the rheology, probably the matrix, is more susceptible to the micrometeoroid abrasion. The clasts are more resistant to micrometeoroids and develop positive reliefs. The topography can be described in terms of

advection, i.e., removal of material with retreat and preservation of slope, and contrasts with the diffusion-like topography typical for monolithic boulders (e.g., Rüsch & Wöhler 2022), where removal of material is associated to a change in slope. This morphology probably develops slowly and is only evident in old (>100 Myr) survivor boulders. The hummocky texture and presence of bright clasts is very similar to the boulder containing intra-boulder bright clasts on Ryugu (Sugimoto et al. 2021) and Bennu (DellaGiustina et al. 2021).

Boulder field with pattern (Figures 6(m)–(p)): Field of nonfractured boulders displaying a radial pattern, e.g., broad and short rays, and a central area lacking boulders. The spatial density of boulders is very high, i.e., boulders can be in contact with each other, and the boulders themselves show no sign of fragmentation. The field is generally wider than the "cluster" type. However, some instances of this group are indistinguishable from the "cluster" type, implying a continuum of morphologies. *Interpretation:* morphology resulting from an impact into a fine-grained target (i.e., regolith) containing large inclusions (i.e., preexisting boulders or fractured bedrock) and different from that of an impact into a target composed of only fine-grained or large particles (e.g., Güttler et al. 2012). The spatially inhomogeneous distribution of boulders around the impact site, i.e., the rays and the pattern, are consistent with laboratory and numerical simulations of impact into a target with a wide range of particle sizes without a dominant particle size (e.g., Kadono et al. 2019, 2020; Raducan et al. 2022b; Ormö et al. 2022). The observed radial pattern is itself the result of filament structure in the ejecta curtain (e.g., Kadono et al. 2022). On the Moon, this morphology indicates the presence of a subsurface rich in boulders or of an underlying pre-fractured bedrock.

4. Discussion

The foundation of this work is a catalog of more than 180,000 fractured feature candidates detected and mapped by a neural network. As the true variety of boulder fragmentation morphologies on the Moon is unknown, any (supervised) machine-learning-driven mapping approach faces a fundamental limitation. We addressed this limitation by purposely training a detector with a very broad perception, enabling it to identify and map known as well as unknown features—where "unknown" features need to be somewhat similar to the "known" features used for training. The overall validity of this approach is underlined by the fact that the detector discovered and mapped a range of previously unknown fractured boulder morphologies (see, e.g., Figure 6). The question of whether the current catalog and descriptions as presented in this work are complete remains open, however. Any quantitative conclusion drawn from this work might suffer from potentially significant bias(es). For example, it remains unclear how significant the discrepancy between the number of detected and actual fractured boulders on the lunar surface is. In addition, it remains unclear whether the model missed specific types of fractured boulders in certain regions of the Moon.

In general, morphologies in cluster 2 as defined by the unsupervised clustering (Section 3.3, Figure 2) might be interpreted in terms of long-lasting landforms such as large fractured survivor blocks belonging to mature (>50–100 Myr) ejecta block fields or to fractured exposed bedrock, e.g., on central peaks of large craters. Morphologies in Cluster 13 might represent short-lived landforms such as smaller fragmented blocks in immature ejecta block fields. For such younger immature ejecta block fields, the larger blocks are not yet fractured or, due to the small size of the crater, are not formed. A comparison between the maps of cluster 2 and 13 with the rock abundance map retrieved from thermal observations by Diviner (Bandfield et al. 2011) demonstrates that rock-rich regions can be very different. For example, regions of relatively similar Diviner rock abundance such as Copernicus (crater interior and ejecta blanket) and Mare Humorum seem to correspond to large (∼20 m) fractured blocks and to small fragments (<10 m) of shattered blocks, respectively (Figure 7). In other words, different SFDs of rocks and different spatial configurations can produce the same rock abundance measured by Diviner. These differences could be used to improve the estimate of rock abundance and surface properties from the Diviner data in future analyses and might enable more detailed studies of the genesis and evolution of boulders on larger spatial scales.

Many of the morphologies detected in the visual survey (Section 3.2) have been described in previous work on rock failure (e.g., Basu et al. 2013; Zhang et al. 2022) or shattering (e.g., Fujiwara et al. 1989; Nakamura et al. 2008; Durda et al. 2015); although, it is the first time that these morphologies are observed for very large target sizes (10–50 m) and for the velocity regime of ∼5–40 km s^{-1} (e.g., Ivanov 2001; McNamara et al. 2004). The similarity of morphological types for impact-induced fragmentation occurs over a wide range of target sizes: centimeters (in laboratory experiments) to tens of meters (reported here). This is consistent with scale invariant fractal flaw distribution (e.g., Turcotte 1997; Housen & Holsapple 1999). Several of the identified morphologies can be grouped in two overarching classes characterized by the flaw geometry: concentric and radial flaws. Based on the geometry of the flaws, we propose that "concentric fracturing" and "near-vertical spalling" are lower-energy modes of the "core" type, characterized by concentric flaws. Instances of radial fracturing present in the "axial failure" type are a lower-energy mode of the "cones" and "no core" types mode, characterized by radial flaws. Importantly, we find that these two flaw geometries, exemplified by the types "cones" and "core" already described in Fujiwara et al. (1989), do not appear to depend on the imparted energy inferred as the ratio size largest fragment/size parent. For example, there are cone modes with the largest fragments having a size of about one-third that of the parent. There are also core modes with the largest fragment (only one) having a size of about one-third that of the parent. This means that for about the same size of the largest fragment, either the cones or core mode could develop. This duality can be observed for high-energy events as well. For example, in two instances of the "cluster" type (Figures 5(e), (f), and reproduced in Figure 8) the ratio Alf/Ap is similar. However, in Figure 5(e) the largest fragments are at the center, whereas in Figure 5(f) the largest fragments are distributed in a near circular pattern. The difference might be due to the impactor property, i.e., difference in velocity or mass for the same imparted energy, and/or target property. This is consistent with suggestions in Giblin et al. (1998) where cone type was generally associated with large and low-velocity impactors and core type to small and high-energy impactors. It is likely that while our observations suggest that one of the two flaw geometries can dominate fragmentation, both types are involved in the process.

There are additional associations that can be established between several of the morphological types. Figure 8 illustrates

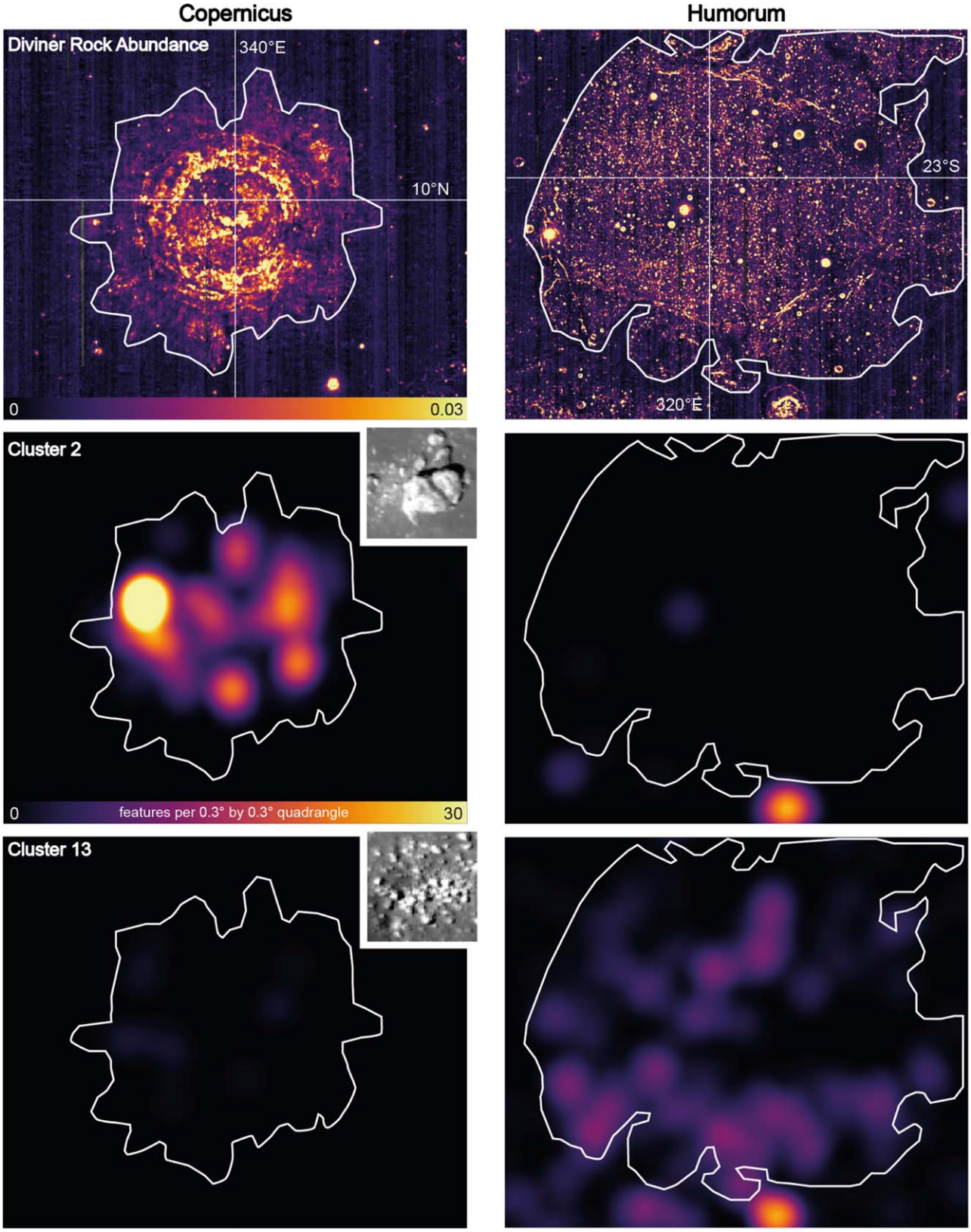

Figure 7. Comparison of Diviner rock abundance maps and cluster 2 and cluster 13 heat maps for the Copernicus crater and Mare Humorum. The fractured features in Copernicus and Mare Humorum seem to correspond to large ($\sim > 10$ m) fractured blocks and to small fragments ($<\sim 7$ m) of shattered blocks, respectively, while featuring relatively similar Diviner rock abundance values.

the fragmentation energy and temporal relationships between morphologies, with solid and dashed lines, respectively. The relationship based on the fragmentation energy described in the preceding paragraph is exemplified by the close-up images on line "a" and "b." The fragmentation energy is qualitatively inferred from the ratio Alf/Ap. The temporal relationship

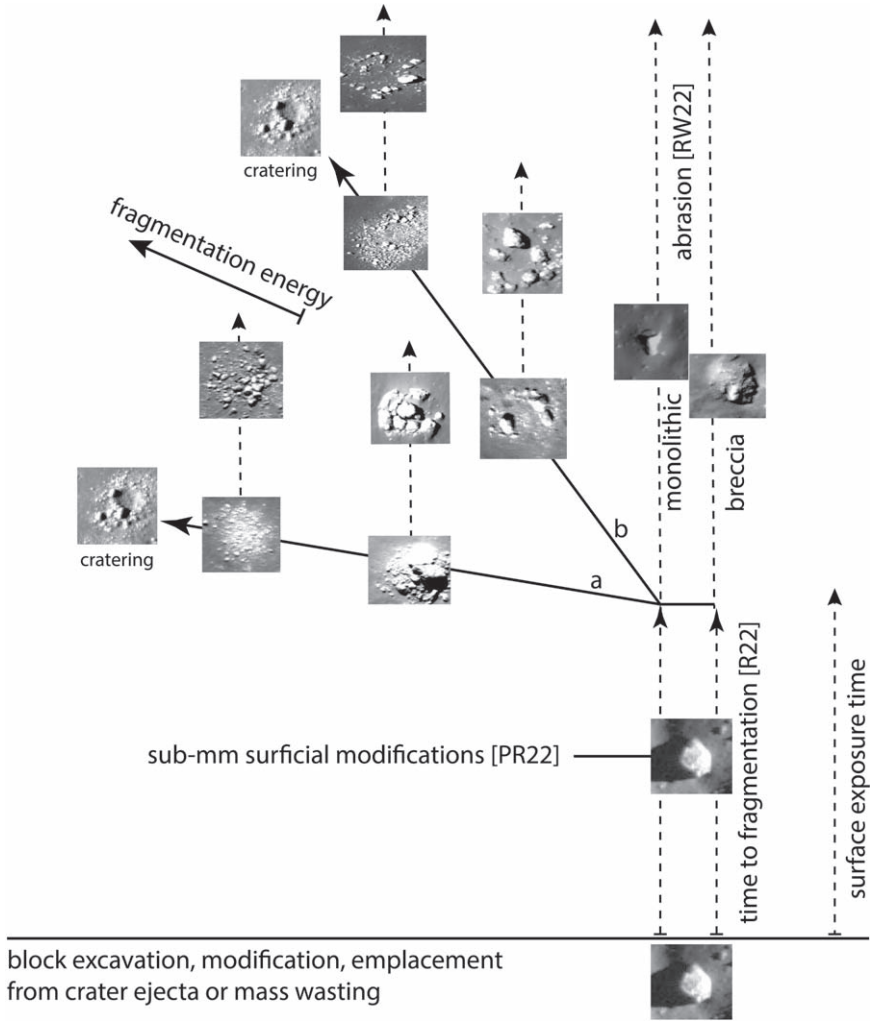

Figure 8. Summary and relationships of lunar boulder morphologies under erosion. Relationships between morphologies can be described in terms of exposure time after emplacement and impact fragmentation energy. Before fragmentation, changes of morphology are limited to submillimeter surficial modifications. After fragmentation (where it occurs), changes of morphology due to increase in exposure age (connected by dashed lines) correspond to a loss of high reflectance, and/or decrease of small fragment number and/or development of debris apron. Lines a and b represent the end-member morphologies of the "core" and "cones" failure types, respectively. Survivor boulders that are not fragmented by a large meteoroid continue to develop debris aprons by abrasion. Specific studies are R22: Rüsch et al. (2022), PR22: Patzek & Rüsch (2022), and RW22: Rüsch & Wöhler (2022). Image credits to NASA/LROC/GSFC/ASU.

between any type of morphology is exemplified by the dashed lines. If small fragments are formed at the time of fragmentation, usually in a high-energy event, their number decreases with time such that only large fragments will remain after a few tens of million years (Rüsch et al. 2022). In addition, very recent events are likely to display a bright surface due to the presence of unresolved fragments (e.g., Marshal et al. 2023) or unweathered particles (e.g., Pieters & Noble 2016). As the close-up images in Figure 8 illustrate, when the exposure age is more than sufficient to erase all small fragments, there is development of a debris apron (fillet) identifiable by a bright halo adjacent to rocks. In the extreme case of a very old exposure age, there is self burial, as described in Rüsch & Wöhler (2022). This is only observed for "survivor" boulders that did not undergo fragmentation.

We note that there exists degeneracy on some of these relationships because it is challenging to determine whether a fragmentation event occurred without formation of small fragments, or whether the small fragments have been erased after their formation. In Figure 8 we interpret the absence of small fragments to be due to their erasure. This is however not necessarily true for all instances. In particular, mild subcatastrophic events, with $\mathrm{Alf}/\mathrm{Ap} > 0.5$, might have been formed without production of small fragments as shown by examples of fragmented blocks with bright zones.

Finally, we detected several instances testifying for very high fragmentation energy where the center of the cluster-type morphology presents a shallow depression. These detections shown in Figure 8 represent the end of the so-called armoring regime and the start of the cratering regime of the underlying surface. This situation is equivalent to the case for rubble-pile surfaces of asteroids where the impact energy is mostly dissipated by the fragmentation of the first-contact block, and little energy is available for crater excavation (e.g., Tatsumi & Sugita 2018; Bierhaus et al. 2022).

As stated earlier, some boulder morphologies on asteroid Bennu have been ascribed to erosion by thermal stresses (e.g., Delbo et al. 2014; Walsh et al. 2019; Molaro et al. 2020). We have detected these same morphologies. The morphology on Bennu described as disaggregation in place with disaggregated fragments on and around the parent block (Molaro et al. 2020) corresponds to the "localized damage" type we detected. The morphology on Bennu described as exfoliation corresponds to

the "near-vertical spalling" type we observed. Another morphology of Bennu described as disaggregation of a clasts-bearing boulder, which leads to highly irregular, hummocky profiles of some Bennu boulders, corresponds to the advection-like erosion we observed for the "breccia" type. These findings could imply that the morphologies on Bennu are formed by meteoroid bombardment and not thermal stresses, or, perhaps less likely, that very different regimes of thermal stresses present on bodies of different dynamical, orbital, and rheological properties (e.g., Molaro et al. 2017; Ravaji et al. 2019; Patzek & Rüsch 2022) lead to the development of similar morphologies. It is also very likely that different processes lead to the development of similar morphologies, thus limiting, in some cases, the inference based on geomorphology alone.

Another argument, presented in Delbo et al. (2022), for the predominant role of thermal stresses in eroding boulders on Bennu is the preferential fracture orientation in planar view. Since the preferentially oriented fractures, supposedly formed by thermal stresses, are more abundant than the randomly oriented fractures formed by impact, it is suggested that fragmentation driven by thermal stresses dominates (Delbo et al. 2022). However, a preferential orientation of fractures has been measured on the Moon as well (Ruesch et al. 2020) where the thermal stresses regime is very different (Molaro et al. 2017) and impact fragmentation dominates (Hörz & Cintala 1997; Hörz et al. 2020; Ruesch et al. 2020; Patzek & Rüsch 2022). This type of fracturing with preferential orientation on the Moon is only one of several modes of failure (Figure 8), and one of relatively little efficiency in terms of mass of the largest fragment to mass of the parent. Failure modes resulting in "core" or "cone" morphologies represent much more efficient modes.

We note that the observed morphologies on asteroids relate to generally smaller ($\sim$3 m) boulders compared to the boulders observed in this study. However, there are several lines of evidence that indicate that in the size range $\sim$1 m to several tens of meters, the size does not have a significant influence on morphologies. In the previous work of Ruesch et al. (2020), no evidence was found for a change of fragmentation morphology with boulder size in the range 8–60 m. In general, there are relatively far fewer examples available of lunar fragmentation morphologies for rocks much smaller than 8 m, limited to in situ images. Nevertheless, the few examples of these smaller-scale morphologies are identical to the larger scale. For example, the near-vertical spall failure mode is observed for a 1 m sized rock at the Apollo 14 site (NASA photograph AS14-68-9445; Hörz et al. 2020). Shear failure mode is observed for a $\sim$2 m sized boulder at the Apollo 16 site (AS17-140-21429HR; Ruesch 2020). Thigh groups of fragments of size 10 and 4 m are observed at the Apollo 14 and Chang'e-3 landing sites (Ruesch 2020), corresponding approximately to the type "cones" or "no core." A $\sim$1 m sized group of fragments displaced in a spatial configuration similar to the type "cluster" is observed near the Chang'e-4 landing site (Figure 2 in Gou et al. 2020). Therefore, there does not appear to be a change in failure mode due to size for the range 1–60 m.

In summary, the observation made in Ruesch et al. (2020) and confirmed here, that most (>80%) of the boulders in a population of any age appear intact (in orbital images) and only few (<20%) are fractured, might imply that the fragmentation process is characterized by a boulder weakening period when the boulder is internally damaged without disruption until sudden shattering occurs with a low Alf/Ap ratio. During the weakening period, the boulder accumulates internal damage due to multiple mild impacts (Rüsch et al. 2022) without displaying morphological signs of damage at the boulder (macro) scale. The length of this internal weakening period is controlled by the meteoroid impact flux, varies stochastically, and increases with increasing boulder size. It can last for up to a few hundreds of million years for boulders >10 m in size. It is likely that, during this period, thermal stresses driven by diurnal temperature variations could lead to additional damage in the interior of the boulder (e.g., Molaro et al. 2017). Furthermore, during this period, the surficial properties of the boulder are modified by micrometeoroid bombardment (Rüsch & Wöhler 2022) and, for petrologies susceptible to thermal stresses, by microcracking and -flaking (Patzek & Rüsch 2022).

5. Conclusion

The boulders located on the surface of the Moon are subject to high-velocity impact fragmentation and thus contribute to regolith formation, enabling the study of fragmentation and regolith development processes. Because of the heterogeneous distribution of boulders—and specifically fractured boulders—across the Moon's surface, we deployed a convolutional neural network to automatically identify and map them in LRO NAC images, effectively creating a global (60°N to S) catalog of fragmented boulders and other features with more than 180,000 entries. The data set is available to the community for further studies. An analysis of the data set allows us to draw the following, qualitative conclusions.

1. Many high-velocity impact fragmentation morphologies can be described in terms of either concentric or radial flaws. In general, we find no obvious, qualitative correlation between the type of morphology and the selenographic position. However, regions of the same rock abundance in Diviner maps might be produced by rocks of different sizes and morphologies.
2. New boulder morphologies are identified. Advection-like morphology is identified as a new type of rock degradation typical for breccia that differs from the more common abrasion-like morphology with a debris apron of monolithic blocks. Impact morphologies for particular conditions (e.g., for a buried boulder, for fine-grained target containing boulders) studied in laboratory or numerical simulations for asteroids are identified for the first time on the Moon and can be studied in this data set while additionally considering the aspect of different gravity between the Moon and small airless bodies.
3. Fragmented rock morphologies interpreted to be due to thermal stress on asteroid Bennu are identified, some for the first time, on the Moon, where the thermal stress regime is different. Therefore, some morphologies might be nondiagnostic in terms of the fracture formation process. In addition, the presence alone of boulder-scale morphological characteristics consistent with thermal stresses does not necessarily imply thermal stresses are the dominant fragmentation and erosion agent on the Moon and on asteroids.
4. Our observations suggest that the fragmentation process on the Moon and possibly on asteroids is characterized by a weakening period with limited macroscopic morphological signs of damage at large scale until sudden catastrophic impact shattering occurs.

Acknowledgments

The LROC team is acknowledged for the acquisition of the images. The constructive comments by two anonymous reviewers improved the clarity of the manuscript and are acknowledged.

References

Arakawa, M., Saiki, T., Wada, K., et al. 2020, Sci, 368, 67
Ballouz, R.-L., Walsh, K. J., Barnouin, O. S., et al. 2020, Natur, 587, 205
Bandfield, J. L., Ghent, R. R., Vasavada, A. R., et al. 2011, JGRE, 116, E00H02
Barnouin, O. S., Daly, R. T., Cintala, M. J., & Crawford, D. A. 2019, Icar, 325, 67
Basu, A., Mishra, D. A., & Roychowdhury, K. 2013, Bull. Eng. Geol. Environ., 72, 457
Bickel, V. T., Aaron, J., Manconi, A., Loew, S., & Mall, U. 2020a, NatCo, 11, 2862
Bickel, V. T., Conway, S. J., Tesson, P. A., et al. 2020b, IJSTA, 13, 2831
Bickel, V. T., Lanaras, C., Manconi, A., Loew, S., & Mall, U. 2018, ITGRS, 57, 3501
Bickel, V. T., Loew, S., Aaron, J., & Goedhart, N. 2022, GeoRL, 49, e98812
Bickel, V. T., Mandrake, L., & Doran, G. 2021a, JPRS, 182, 1
Bickel, V. T., Mandrake, L., & Doran, G. 2021b, Frontiers in Remote Sensing, 2, 4
Bierhaus, E. B., Trang, D., Daly, R. T., et al. 2022, NatGe, 15, 440
Bruno, D. E., & Ruban, D. A. 2017, P&SS, 135, 37
Cambioni, S., Delbo, M., Poggiali, G., et al. 2021, Natur, 598, 49
Cambioni, S., Delbo, M., Ryan, A., Furfaro, R., & Asphaug, E. 2019, Icar, 325, 16
Capaccioni, F., Cerroni, P., Coradini, M., et al. 1986, Icar, 66, 487
Cintala, M. J., Berthoud, L., & Hörz, F. 1999, M&PS, 34, 605
Daly, R. T., Ernst, C. M., Barnouin, O. S., et al. 2023, Natur, 616, 443
Delbo, M., Libourel, G., Wilkerson, J., et al. 2014, Natur, 508, 233
Delbo, M., Walsh, K. J., Matoni, C., et al. 2022, NatGe, 15, 453
DellaGiustina, D. N., Emery, J. P., Golish, D. R., et al. 2019, NatAs, 3, 341
DellaGiustina, D. N., Kaplan, H. H., Simon, A. A., et al. 2021, NatAs, 5, 31
Di, K., Xu, B., Peng, M., et al. 2016, P&SS, 120, 103
Durda, D. D., Bottke, W. F., Nesvorny, D., et al. 2007, Icar, 186, 498
Durda, D. D., Campo Bagatin, A., Aleman, R. A., et al. 2015, P&SS, 107, 77
Durda, D. D., Chapman, C. R., Cintala, M. J., et al. 2011, M&PS, 46, 149
Dutro, J. T. J., Dietrich, R. V., & Foose, R. M. 1989, AGI Data Sheets: For Geology in the Field, Laboratory, and Office (3rd ed.; Alexandria, VA: American Geological Inst.)
Fujiwara, A., Cerroni, P., Davis, D. R., et al. 1989, Asteroids II (Tucson, AZ: Univ. Arizona Press), 240
Fujiwara, A., & Tsukamoto, A. 1980, Icar, 44, 142
Giblin, I., Martelli, G., Farinella, P., et al. 1998, Icar, 134, 77
Giblin, I., Martelli, G., Smith, P. N., et al. 1994, Icar, 110, 203
Gou, S., Yue, Z., Di, K., et al. 2020, JGRE, 126, e06565
Güttler, C., Hirata, N., & Nakamuira, A. M. 2012, Icar, 220, 1040
Hogan, J. D., Rogers, R. J., Spray, J. G., & Boonsue, S. 2012, Engineering Fracture Mechanics, 79, 103
Hörz, F., Basilevsky, A. T., Head, J. W., & Cintala, M. J. 2020, P&SS, 194, 105105
Hörz, F., & Cintala, M. 1997, M&PS, 32, 179
Hörz, F., Schneider, E., Gault, D. E., Hartung, J. B., & Brownlee, D. E. 1975, Moon, 13, 235
Housen, K. R., & Holsapple, K. A. 1990, Icar, 84, 226
Housen, K. R., & Holsapple, K. A. 1999, Icar, 142, 21
Ivanov, B. A. 2001, in Chronology and Evolution of Mars. Series: Space Sciences Series of ISSI, ed. R. Kallenbach, J. Geiss, & W. K. Hartmann (Dordrecht: Springer), 87
Kadono, K., Suetsugu, R., Arakawa, D., et al. 2019, ApJL, 880, L30
Kadono, K., Suzuki, A. I., Matsumara, R., et al. 2020, Icar, 339, 113590
Kadono, K., Suzuki, A. I., Suetsugu, R., et al. 2022, EP&S, 74, 128
Kodikara, G., & McHenry, L. 2020, Icar, 345, 113719
Kun, F., & Herrmann, H. J. 1999, PhRvE, 59, 2623
Lauretta, D. S., Adam, C. D., Allen, A. J., et al. 2022, Sci, 377, 285
Li, C., Liu, J., Ren, X., et al. 2015, SSRv, 190, 85
Li, Y., & Wu, B. 2018, JGRE, 123, 1061
Lin, T. Y., Goyal, P., Girshick, R., He, K., & Dollár, P. 2017, arXiv:1708.02002
Marshal, R. M., Rüsch, O., Wöhler, C., et al. 2023, Icar, 394, 115419
Matsui, T., Waza, T., Kani, K., & Suzuku, S. 1982, JGR, 87, 10968
McNamara, H., Jones, J., Kauffman, B., et al. 2004, EM&P, 95, 123
Molaro, J. L., Byrne, S., & Le, J.-L. 2017, Icar, 294, 247
Molaro, J. L., Walsh, K. J., Jawin, E. R., et al. 2020, NatCo, 11, 2913
Moseley, B., Bickel, V. T., Burelbach, J., & Relatores, N. 2020, PSJ, 1, 32
Nakamura, A. M., MIchikami, T., Hirata, N., et al. 2008, EP&S, 60, 7
Okawa, H., Arakawa, M., Yasui, M., et al. 2022, Icar, 387, 115212
Ormö, J., Raducan, S. D., Jutzi, M., et al. 2022, E&PSL, 594, 117713
Patzek, M., & Rüsch, O. 2022, JGRE, 127, e2022JE007306
Pieters, C. M., & Noble, S. K. 2016, JGRE, 121, 1865
Raducan, S. D., Davison, T. M., & Collins, G. S. 2022a, Icar, 374, 114793
Raducan, S. D., Jutzi, M., Zhang, Y., Ormö, J., & Michel, P. 2022b, A&A, 665, L10
Ravaji, B., Alí-Lagoa, V., Delbo, M., & Wilkerson, J. W. 2019, JGRE, 124, 3304
Robinson, M. S., Brylow, S. M., Tschimmel, M., et al. 2010, SSRv, 150, 81
Ruesch, O. 2020, LPSC, 51, 2118
Ruesch, O., Sefton-Nash, E., Vago, J. L., et al. 2020, Icar, 336, 113431
Rüsch, O., Marshal, R. M., Iqbal, W., et al. 2022, Icar, 387, 115200
Rüsch, O., & Wöhler, C. 2022, Icar, 384, 115088
Ryan, E. V., & Melosh, J. 1998, Icar, 133, 1
Stickle, A. M., DeCoster, M., Burger, C., et al. 2022, PSJ, 3, 248
Sugimoto, C., Tatsumi, E., Cho, Y., et al. 2021, Icar, 369, 114529
Tanga, P., Cellino, A., Michel, P., et al. 1999, Icar, 141, 65
Tatsumi, E., & Sugita, S. 2018, Icar, 300, 227
Thomas, P. 1979, Icar, 40, 223
Turcotte, D. L. 1997, Fractals and Chaos in Geology and Geophysics (Cambridge: Cambridge Univ. Press)
Walker, J. D., Chocron, S., Durda, D. D., et al. 2013, IJIE, 56, 12
Walsh, K. J., Ballouz, R.-L., Jawin, E. R., et al. 2022, SciA, 8, eabm6229
Walsh, K. J., Jawin, E. R., Ballouz, R.-L., et al. 2019, NatGe, 12, 242
Wilhelms, D. E., McCauley, J. F., & Trask, N. J. 1987, The Geologic History of the Moon Professional Paper 1348, USGS
Zhang, P., Wu, Z., Sun, J., et al. 2022, PLoSO, 17, e0266241